Catalysis Science & Technology

Selectivity Enhancement in Electrochemical Reduction of Oxalic Acid on Titanium Dioxide Nanoparticles Achieved by Shape and Energy-states Controls

Journal:	*Catalysis Science & Technology*
Manuscript ID	CY-ART-07-2021-001239.R2
Article Type:	Paper
Date Submitted by the Author:	26-Sep-2021
Complete List of Authors:	Eguchi, Hiroto; Kyushu University, Department of Chemistry, Gradate school of Science Kato, Kenichi; JARSI/SPring-8, Juhász, Gergely; Tokyo Institute of Technology, Department of Chemistry, Graduate School of Science Yamauchi, Miho; Kyushu University, I2CNER

COMMUNICATION

Selectivity Enhancement in Electrochemical Reduction of Oxalic Acid on Titanium Dioxide Nanoparticles Achieved by Shape and Energy-states Controls

Received 00th January 20xx,
Accepted 00th January 20xx

DOI: 10.1039/x0xx00000x

Hiroto Eguchi,[a] Kenichi Kato,[b] Gergely Juhasz[c, *], and Miho Yamauchi [a, d, e, *]

We applied various shape-controlled TiO_2 nanoparticles (NPs) for the electrochemical reduction to produce an alcoholic compound. Catalytic activity depended on the shape of TiO_2 NPs. Computational studies and extensive characterization suggest that high efficiency and selectivity can be achieved on the TiO_2 NPs utilizing a combination of {001} and {101} facets.

Electrochemical reactions can directly convert electric power generated from renewable energies, i.e., renewable electricity, into chemical energy stored in molecules, which are called energy carriers.[1] Therefore, efficient and selective electrochemical reactions play a crucial role to promote the common use of renewable electricity and to solve current energy-related issues.

In general, metal catalysts such as Pt[2], Cu[3], and Au[4] are used as a cathode to produce energy carriers.[5-7] Recently, we found that anatase type TiO_2 catalysts can be used for highly selective electro-reduction of oxalic acid (OX), a divalent carboxylic acid, to produce glycolic acid (GC), a monovalent alcoholic compound, via 4-electron reduction, which enables direct electric power storage into easily storable and transportable GC as an energy carrier.[8-14] Noted that hydrogen evolution is remarkably suppressed over TiO_2 even in highly acidic aqueous OX solution, i.e., TiO_2 has a wide potential window in aqueous media. However, the enhancement of catalytic activity on oxide catalysts is still a significant challenge for the practical use. Various efforts have been implemented to achieve the higher activity on an electrocatalyst, e.g., doping a different element,[15] reducing size into the nanoscale,[16] and controlling oxidation states.[17] The shape and facets of catalysts can also significantly influence the activity in the photo- and electrochemical reactions.[18-20] For example, needle-like shapes of metal particles contribute to the concentration of the electric field, which considerably promotes catalytic performances.[21] In contrast, the influence of the shape for the electrocatalytic reaction on oxides is not fully clarified yet whereas their shapes of metal nanoparticles (NPs) catalysts vary their performances in many cases. Herein, we examine the influence of the shape of TiO_2 NPs on the electrochemical OX reduction by comparison with various characteristics of TiO_2 NPs, such as electronic states and morphology and elucidate the relevance between electrocatalytic performances and shape-dependent electronic states of oxides, i.e., energy levels of conduction band bottom (CBB) and valence band top (VBT), for the first time as far as we know. For better understanding of the findings, we have also performed computational studies based on Density Functional based Tight Binding (DFTB) method on TiO_2 NP models. We found that the electrons can be localized around proximity of the apex due to the emergence of localized electronic states for NPs. These localized states may explain the shape-dependent activity and the catalytic enhancement on the NPs exhibiting high density of apex. Furthermore, mixing of specific facets on NPs resulted in high selectivity for the OX reduction on TiO_2 NPs.

Characterization of the TiO_2 NPs

We prepared six TiO_2 nanoparticle samples from a titanate precursor using solvothermal methods according to previously reported procedures[22–28] A series of the series of shape-controlled TiO_2 NPs, such as a columnar truncated bipyramidal decahedron exposed {101} facets (101-column), a truncated bipyramidal decahedron exposed {101} facets (101-deca), a truncated bipyramidal decahedron exposed {001} facets (001-deca), a sphere condensed sheet exposed {001} facets (001-sheet-C), a sphere stacked sheet exposed {001} facets (001-sheet-S), a truncated asymmetric bipyramidal decahedron exposed {201} facets (201-deca). The detailed synthetic

[a.] *Department of Chemistry, Graduate School of Science, Kyushu University, 744 Motooka, Nishi-ku, Fukuoka, Japan.*
[b.] *RIKEN SPring-8 Center, 1-1-1 Kouto, Sayo-cho, Sayo-gun, Hyogo, Japan.*
[c.] *Department of Chemistry, Graduate School of Science, Tokyo Institute of Technology, 2-12-1 Ookayama, Meguro-ku, Tokyo, Japan.*
[d.] *International Institute for Carbon-Neutral Energy Research (WPI-I²CNER), Kyushu University, 744 Motooka, Nishi-ku, Fukuoka, Japan.*
[e.] *Advanced Institute for Materials Research (AIMR), Tohoku University, 2-1-1 Katahira, Aoba-ku, Sendai, 980-8577, Japan*
Electronic Supplementary Information (ESI) available: [details of any supplementary information available should be included here]. See DOI: 10.1039/x0xx00000x

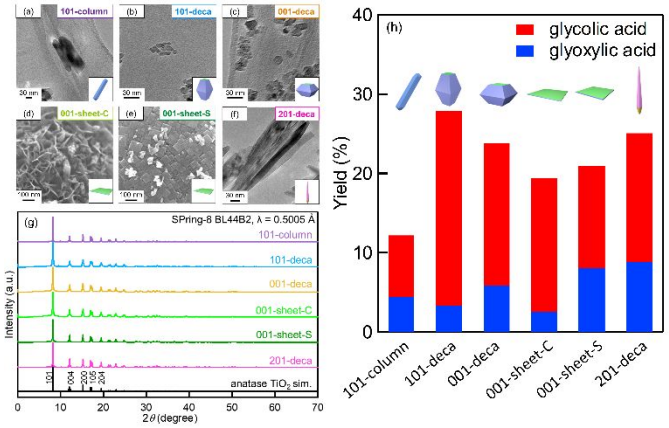

Figure 1 TEM images of (a) 101-column, (b) 101-deca, (c) 001-deca, (f) 201-deca, and SEM images of (d) 001-sheet-C, (e) 001-sheet-S. (g) XRD patterns of the TiO_2 NPs prepared by solvothermal synthesis. (h) Yield for electrochemical reduction of OX on shape-controlled TiO_2 NPs. The CA measurement was carried out at −0.7 V vs. RHE and 50 °C for 2 hours. The iR correction was not performed and the reference electrode was not calibrated to the temperature.

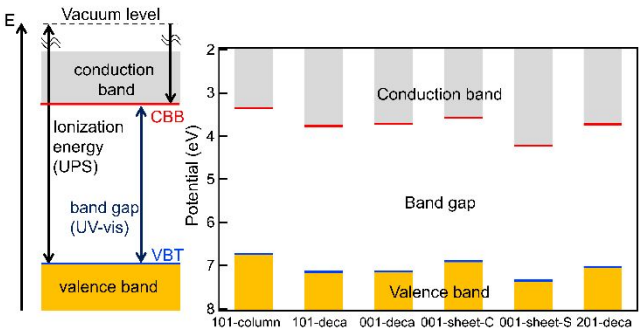

Figure 2 Energy levels of conduction band bottom (CBB) and valence band top (VBT) of TiO_2 NPs.

procedure is provided in electronic supplementary information (ESI).

. As shown in Figure 1 (a)-(f), the TEM and SEM measurements revealed that TiO_2 samples have a specific shape surrounded with particular facets.

X-ray diffraction (XRD) patterns for all of prepared TiO_2 NPs represented NPs are well-crystallized anatase type TiO_2 (Figure 1 (g)) and Rietveld analyses for the XRD patterns provided detailed structural parameters for the prepared sample (Figure S1 and Table S1).[29] X-ray photoelectron spectroscopy (XPS) for TiO_2 NPs were conducted to evaluate the electronic states of TiO_2 NPs. XPS survey spectra and high-resolution XPS spectra for Ti2*p* and O1*s* of TiO_2 NPs, as shown in Figures S2-S4, revealed that the valence states of Ti and O included in prepared TiO_2 NPs are almost the same.

Catalytic performance for electrochemical reduction on shape controlled TiO_2 NPs

We conducted cyclic voltammetry (CV) experiments and Tafel analysis on the TiO_2 NPs loaded on Ti foil electrodes to evaluate their catalytic activity (Figure S5). The reduction current in the OX solution is larger than the blank solution for all TiO_2 NPs. Thus, the reduction of oxalic acid occurred in all TiO_2 NPs. In addition, the Tafel plots are composed of multiple elementary reactions including hydrogen evolution because there are tiny steps in the Tafel plot between 0 and −0.5 V vs. Ag/AgCl. The electrochemical reduction of oxalic acid proceeds via steps of 2-electron reductions, which is accompanied by the formation of glyoxylic acid (GO) as shown below. [10]

$(COOH)_2 + 2\ H^+ + 2\ e^- \rightarrow HOOC\text{-}COH + H_2O$

$HOOC\text{-}COH + 2\ H^+ + 2\ e^- \rightarrow HOOCCH_2OH$

Considering that hydrogen evolution also simultaneously occurs, the Tafel plots are possibly composed of multiple elementary reactions and cannot be easily resolved.

To examine product distribution on TiO_2 NPs, we performed chronoamperometry (CA) experiments on TiO_2 NPs. Figures 1 (h) and S6 show that electro-reduction of OX to GC and GO and generation of H_2 occurs in the reaction whereas the selectivity for OX reduction seems smaller compared to those reported in our previous results using micro-meter scale TiO_2 catalysts.[8, 12] This possibly suggests that the size of TiO_2 catalysts also influences the product selectivity. More importantly, both selectivity and Faradaic yields for products were strongly affected by the shape of TiO_2 NPs. The highest selectivity for GC production was 61% in the experiment, which was achieved on 101-deca. Selectivity for the production of GC on 001-sheet-C and 001-sheet-S, which are largely exposed to {001} facets, and on 101-column, of which surface is covered with both {001} and {101} facets, were considerably low. In contrast, NPs having particular surfaces composed of {001} and {101} facets, i.e. 101-deca and 001-deca, showed much higher selectivity for the GC production.

Influential factors on catalytic activity

Then, we focused on the factor that influences the catalytic activity, i.e., yield. We evaluated the relationship between product yield and the surface area of TiO_2 NPs, which is related to the number of active sites. Figure S7 shows the nitrogen adsorption-desorption curves. Figure S8 represents that the BET specific surface area, which was calculated from the curves shown in Figure S7. BET specific surface area was found to depend on the shape of TiO_2 NPs, e.g. 001-sheet-C and 201-deca exhibited the largest and smallest BET specific surface area 101 $m^2\ g^{-1}$ and 19 $m^2\ g^{-1}$, respectively. In contrast, we observed no clear relationship between the yields and the specific surface area, suggesting that the active sites on TiO_2 NPs are not evenly distributed on the surface of TiO_2 NPs (Figure S9). This result suggests the possibility of the preferential active site on specific parts of the NP surfaces.

TiO_2 NPs are a semiconductor and, therefore, their electric conductivity may modify activity for the electrochemical reduction. The temperature dependence of the electronic conductivity of TiO_2 NPs was examined by AC impedance measurements (Figure S10). Further, the relationship between yield for GC and conductivity of TiO_2 NPs is shown in Figure S11. The moderate electronic conductivity (10^{-11} S cm^{-1}) exhibits higher yields for GC, however, we could not see strong correlation between the conductivity of the TiO_2 NPs and the yield.

Under the application of a voltage exceeding overpotentials, electrons move from the state located around CBB of TiO_2 NPs to OX[8, 11, 12, 13, 14], so the absolute position of the conduction

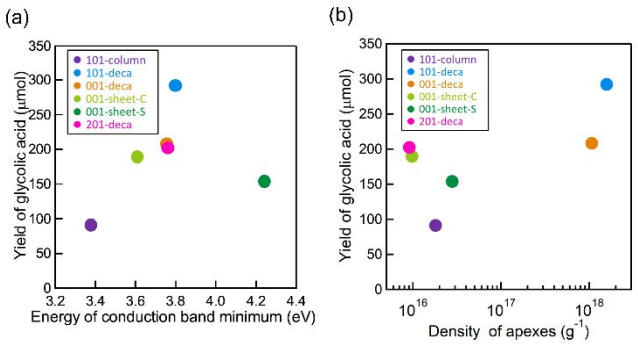

Figure 3 (a) The relationship between the energy level of conduction band bottom (CBB) of TiO_2 NPs and the yields of glycolic acid (GC). (b) The relationship between the density of apexes of TiO_2 NPs and the yields of glycolic acid (GC).

band is possibly important. To evaluate the energy levels of CBB, we measured ultraviolet photoelectron spectroscopy (UPS) spectra of TiO_2 NPs as shown in Figure S12 and UV-visible absorption spectroscopy (Figure S13). The absorption edges in UV-visible spectra for the TiO_2 NPs were located between 360 nm and 400 nm, which is consistent with band gap energies reported for TiO_2 NPs.[30] Figure 2 shows the determined energy levels of CBB and VBT for shape controlled TiO_2 NPs. Interestingly, the CBB levels were found to depend on the shape of TiO_2 NPs. Figure 3(a) shows the yields of GC plotted to the energy level of CBB. We can see the volcanic relation between the energy levels of CBB and the catalytic activity for OX reduction. When the *n*-type semiconductor electrode contacts the aqueous electrolyte solution including reactant molecules, the conduction band of the semiconductor distorts so that the Fermi level of the semiconductor and the redox potential of the solution become equal, resulting in the formation of built-in potential as shown in Figure S14a, b.[31] The difference between the CBB level and the redox potential can be regarded as driving force for the electrochemical reduction, i.e., reduction power. Meanwhile, the hydrogen production is also enhanced on the semiconductor having sufficiently high CBB levels, which leads to the lower Faradaic efficiency for the OX reduction. In this study, we applied sufficiently large negative potential for the reaction and the CBB level is reflected to the catalytic activity (Figure S14c). Therefore, the optimal energy level of CBB for OX reduction can exist, which is consistent with our reports [8, 11, 12, 13, 14].

Effect of apexes on catalytic activity

To clarify the influence of energy level of CBB and consider the other factors, we have performed a series of calculations to simulate the position of bands in anatase nanoparticle models, **NP 1**, **2**, and **3**. Previously, we have calculated band gaps of anatase NPs with different shape and found only little variation for the most stable geometries.[32] While there is a difference between calculated and experimental bandgap values, DFT and DFTB-based calculations are well known for such an error. Such calculations, however, still useful for the discussion of electronic states in oxide NPs. The different band energies in different nanoparticles were partly ascribed to the low energy LUMO states (localized conduction band bottom) around

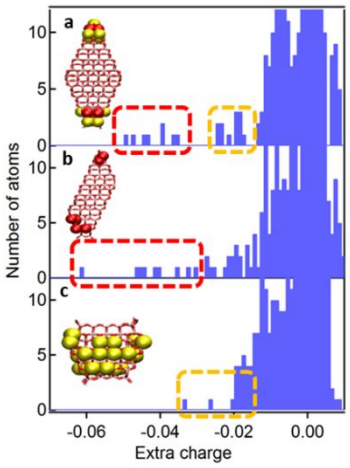

Figure 4 The extra negative charge on different atoms on NP 1 (a), 2 (b) and 3 (c). Red and yellow spheres are indicating the Ti atoms with large extra negative charges corresponding to the range as shown in the histogram.

apexes. These localized LUMO states originate from *d* orbitals of Ti (IV) ions with low coordination numbers. However, not all the low-coordination Ti (IV) ions contribute to the LUMO in the same way, and bond angles and the coordination of neighbouring Ti ions also can influence the localization of these states. This behaviour is similar to Au nanoparticles, where high activities can be observed on curved edges for electrochemical CO_2 reduction.[21]

To study the possible effects of localized frontier states on the electrons during the electrochemical reaction are affected by these localized states, we performed calculations on **NPs 1** and **3** and the columnar NP (**NP 2**). These models have a mixture of {101} and {001} facets to mimic the regular, 101-column, 101-deca, and 001-deca NPs (Figure S15). We compared the charge distribution of neutral and one-electron-reduced NPs and found very strong charge localization emerging around apexes on **NPs 1** and **2**, but not in the case of **NP 3** (See Figure S16 and S17). When we compare the charge distribution of reduced (extra electron) and oxidized (extra hole) nanoparticles, it is clear that the localization is much more pronounced for the lowest energy empty states at CBB where the extra electron can reside (Figure S16). This localization of extra electrons is a result of the localized LUMO states, which mostly consist of *d* orbitals of Ti with 4- and 5- coordination. The LUMO of the nanoparticles consists of Ti *d* orbitals. When we compare the PDOS of these nanoparticles, the Ti ions in the apex region of **NPs 1** and **2** (with 4- and 5- coordination) have a very high contribution to the lowest energy LUMO states (See Figure S18 and S19), and therefore they are acting as trapping sites for extra electrons. Charge trapping in TiO_2 has already been studied, mostly in relationship to photochemical behavior.[33, 34] The role of similar charge trapping in electrochemical properties and the relationship between trapping and crystal morphology is far less explored field.

By removing the apex and creating a new {001} surface these trapping sites can be removed for **NP 3** (See Figure S20), the {001} surfaces and neighbouring edges exhibit similar energy as the states on {101} surfaces. We monitored the

distribution of extra electrons as the difference of Mulliken charges upon reduction of the NP by one electron as it is shown in Figure 4. There are several atoms with extra charge exceeding −0.02, even −0.03, on **NPs 1** and **2**, and these atoms are located on the peak areas as seen in Figure 4, indicating that the charge is indeed trapped in a relatively small surface area. These NPs cannot utilize their whole {101} faces for electrochemical reduction, only a very small part around their apexes. In contrast, the negative charge is much more evenly distributed on the atoms located over {101} surfaces in the case of **NP 3**, providing a wide surface capable of the electro-reduction. The strong absorption of inactive form and the little extra charge on the {001} surfaces suggest that they do not actively participate in the reduction reaction.

To examine the possibility that the active sites are partly localized around apexes, we closely evaluated the relationship between the shape of TiO_2 NPs and catalytic activity. We used simple geometric models constructed based on TEM and SEM images to estimate the density of apexes on the surface (Figure S21). Figure 3(b) shows the relationship between the density of apexes and the yields for GC on the surface of TiO_2 NPs. We can see a tendency that the catalyst having a higher density of apexes on the surface shows a higher conversion of OX. This result corresponds to the result that apexes of TiO_2 NPs, where electrons are trapped, can be the active site for the electrochemical reduction of OX. In addition, the energy levels of CBB partially reflect the energy states of trapping sites around an apex and the junction of {101} and {001} facets because the localized states are located below the CBB level. Thus, the simulations can predict that the reactivity of particles with {101} facets is higher around their apexes, due to the charge trapping. By capping these particles and introducing new {001} facets help to create more active centers on {101} surfaces, which also leads to more apexes. The limited availability of the faces for electrochemical reactions also explains why BET specific surface area does not correlate with the electrochemical activity.

Effect of facets on selectivity

Next, we focus more on the influential factors on selectivity and discuss on activation energies on facets. Previously, we found that {101} surface binds OX via one of the carboxylic groups, which remains electrochemically inactive and reduction can occur only on the non-bound group.[11] When OX absorbed on {001} surface, both carboxylic groups can be strongly tied to the surface, which is the electrochemically inactive form (see in Figure S22). This inactive form binds more than 160 kJ/mol stronger than any active form, making the {001} facets electrochemical activity low. On {101} surface, such double-bound absorption is 49 kJ/mol weaker than the electrochemically active form. Therefore, one would expect NPs with pure {101} superior to NPs with mixed {101} – {001} faces, which is clearly not the case. We also examined whether there are other factors that influence the absorption of OX on the NP surfaces by comparing the absorption energies on different faces and edges on models for octahedral (**NP 1**) and decahedral (**NP 3**) NPs (Figure S23 and S24). The absorption energies for electrochemically active OX geometries on {101} faces and edges are similar to the energies calculated for slab surfaces and somewhat smaller for {001} faces, but these are not substantial differences that would influence the activity. Hence, selective OX absorption on {101} and {001} facets cannot explain the observed selectivity differences.

In contrast, the extra negative charge as shown in Figure 4 also explain the difference in selectivity: the potential on different parts of the electrochemically active surface varies significantly on **NP 1** and **NP 2**, offering active sites for different reactions with slightly different electrochemical potential. On the other hand, the active surface of **NP 3** offers more uniform active sites for the reduction process. We considered exposure and connection of two facets, {101} and {010}, (as found in 101-deca and 001-deca) are the most important factors for the selective OX reduction. H_2 evolution is supposed to require the absorption of several –OH/–OH_2 ligands on the active sites and the 4-coordinated Ti ions in apexes shown on **NPs 1** and **2** probably have a large contribution to H_2 production. By exchanging these highly active apexes with {001} faces and pushing the electrons to {101}, **NP 3** can significantly reduce the unwanted H_2 production and favour OX reduction.

Conclusions

In summary, we have for the first time given a detailed analysis of the effect of the shape of TiO_2 NPs on catalytic performances for electrochemical OX reduction using experimental and theoretical studies. We found that trivial explanations, like difference in conductivity or surface area, cannot fully describe the difference in electrochemical activity and selectivity. We also found that activities and selectivity on TiO_2 NPs were correlated with the energy level of CBB and the density of apexes. Our calculation showed that the {101} surface around the apexes on TiO_2 NPs are the main active site for the electrochemical reduction of OX. These calculations suggested that the electrons participating in the reduction are trapped in lower energy localized LUMO states of the NPs and that apexes on 101-column can act as a catalytic center both for the hydrogen production and the OX reduction. The calculations also revealed that shape-control like capping the NPs with {001} surfaces to form NPs like 101-deca and 001-deca can counterbalance the trapping, and help the delocalization of charge over broader surface areas. Furthermore, the junction of {101} and {001} facets play a significant role for the high product selectivity. Our findings are the first systematic insights concerning selectivity enhancement for the electrochemical reduction of a carboxylic acid on oxide catalysts, which will inspire the development of highly efficient and selective electrocatalysts composed of a wide range of materials.

Acknowledgements

This work was supported by MEXT KAKENHI Grant Number JP18H05517, JP19K22205 and JST-CREST, Japan. The

computations were performed using Research Center for Computational Science, Okazaki, Japan.

Author Contributions

Hiroto Eguchi: Conceptualization, Investigation, Writing-original draft preparation, Kenichi Kato: Methodology, Gergely Juhasz: Software, Writing-original draft preparation, Miho Yamauchi: Conceptualization, Supervision, Writing and editing

Conflicts of interest

There are no conflicts to declare.

References

1 H. Chen, T. N. Cong, W. Yang, C. Tan, Y. Li, Y. Ding, Prog. *Nat. Sci.*,2009, **19**, 291.
2 K. A. Striebel, F. R. McLarnon, E. J. Cairns, *J. Electrochem. Soc.*, 1990, **137**, 3351.
3 Y. Hori, K. Kikuchi, S. Suzuki, *Chem. Lett.*, 1985, **14**, 1695.
4 Y. Hori, H. Wakebe, T. Tsukamoto, O. Koga, *Electrochim. Acta*, 1985, **39**, 1833.
5 S. Sun, D. Liu, G. T. R. Palmore, *ACS Catal*., 1985, **4**, 3091.
6 Z. Wang, G. Yang, Z. Zhang, M. Jin, Y. Yin, *ACS Nano*, 2016, **10**, 4559.
7 Z. Xue, S. Zhang, Y. Lin, H. Su, G. Zhai, J. Han, Q. Yu, X. Li, M. Antonietti, J. Chen, *J. Am. Chem. Soc.*, 2019, **141**, 14976.
8 R. Watanabe, M. Yamauchi, M. Sadakiyo, R. Abe, T. Takeguchi, *Energ. Environ. Sci.*, 2015, **8**, 1456.
9 M. Sadakiyo, S. Hata, X. Cui, M. Yamauchi, *Sci. rep.*, 2019, 7, 17032.
10 T. Fukushima, S. Kitano, S. Hata, M. Yamauchi, *Sci. Technol. Adv. Mat.*, 2018, **19**, 142.
11 M. Sadakiyo, S. Hata, T. Fukushima, G. Juhász, M. Yamauchi, *Phys. Chem. Chem. Phys.*, 2019, **21**, 5882.
12 M. Yamauchi, S. Hata, H. Eguchi, S. Kitano, T. Fukushima, M. Higashi, M. Sadakiyo, K. Kato, *Catal. Sci. Techol*. 2019, **9**, 6561.
13 M. Yamauchi, *Chem*. *Lett*., doi.org/10.1246/cl.210454, in press.
14 K. Fukutani, J. Yoshinobu, M. Yamauchi, T. Shima, S. Orimo, Cat. Lett., doi.org/10.1007/s10562-021-03750-1, in press.
15 E. L. Miller and R. E. Rocheleau, *J. Electrochem. Soc.*, 1997, **144**, 3072.
16 A. Salimi, E. Sharifi, A. Noorbakhsh, S. Soltanian, *Biophys. Chem.*, 2007, **125**, 540.
17 M. Le, M. Ren, Z. Zhang, P. T. Sprunger, R. L. Kurtz, J. C. Flake, *J. Electrochem. Soc.*, 2011, **158**, E45.
18 J. Yu, J. Low, W. Xiao, P. Zhou, M. Jaroniec, *J. Am. Chem. Soc.*, 2014, **136**, 8839.
19 N. Murakami, Y. Kurihara, T. Tsubota, T. Ohno, *J. Phys. Chem. C*, 2009, **113**, 3062.
20 C. Liu, A. Y. Zhang, D. N. Pei, H. Q. Yu, *Environ. Sci. technol.*, 2016, **50**, 5234.
21 M. Liu, Y. Pang, B. Zhang, P. De Luna, O. Voznyy, J. Xu, X. Zheng, C. T. Dinh, F. Fan, C. Cao, *Nature*, 2016, **537**, 382.
22 J. Chen, H. B. Yang, J. Miao, H.-Y. Wang, B. Liu, *J. Am. Chem. Soc.*, 2014, **136**, 15310.
23 W. Q. Wu, H. S. Rao, Y. F. Xu, Y. F. Wang, C. Y. Su, D. B. Kuang, *Sci. Rep.*, 2013, **3**, 1892.
24 Z. Wang, K. Lv, G. Wang, K. Deng, D. Tang, *Appl. Catal. B*, 2010, **100**, 378.
25 B. Wang, X. Zhang, H. Meng, H. Tao, *J. Nanosci. Nanotechno.*, 2013, **13**, 356.
26 J. S. Chen, Y. L. Tan, C. M. Li, Y. L. Cheah, D. Luan, S. Madhavi, F. Y. C. Boey, L. A. Archer, X. W. Lou, *J. Am. Chem. Soc.*, 2010, **132**, 6124.
27 Z. Zhao, Z. Sun, H. Zhao, M. Zheng, P. Du, J. Zhao, H. Fan, *J. Mater. Chem.*, 2012, **22**, 21965.
28 H. B. Wu, J. S. Chen, X. W. David Lou, H. H. Hng, *Nanoscale*, 2011, **3**, 4082.
29 K. Kato, Y. Tanaka, M. Yamauchi, K. Ohara, T. Hatsui, J. Synchrotron Radiat., 2019, **26**, 762-773.
30 K. M. Reddy, S. V. Manorama, A. R. Reddy, *Mater. Chem. Phys.*, 2003, **78**, 239.
31 A. M. Fajardo and N. S. Lewis, *J. Phys. Chem. B*, 1997, **101**, 11136-11151
32 G. Juhasz, *ECS Trans.*, 2018, **85**, 3.
33 K. Shirai, G. Fazio, T. Sugimoto, D. Selli, L. Ferraro, K. Watanabe, M. Haruta, B. Ohtani, H. Kurata, C. Di Valentin, Y. Matsumoto, *J. Am. Chem. Soc.*, 2018, **140**, 1415.
34 F. Nunzi, S. Agrawal, A. Selloni, F. De Angelis, *J. Chem. Theory Comput.,* 2015, **11,** 635.